Exploring a modular adaptive metastructure concept inspired by muscle's cross-bridge

Z Wu, RL Harne and KW Wang

Abstract

The multifunctionality and versatility of skeletal muscle is a worthy inspiration towards the development of engineered adaptive structures and material systems. Recent mechanical modeling of muscle suggests that some of muscle's intriguing macroscale, passive adaptivity results from the assembly of nanoscale, cross-bridge constituents that maintain multiple metastable configurations. Inspired by the new observations, this research explores a concept of creating modular, engineered structures from the assembly of mechanical, metastable modules, defined as modules that exhibit coexistent metastable states. The proposed integrated systems are termed metastructures: modular, engineered structures exhibiting unprecedented characteristics resulting from a synergy of the constituents. Analytical and experimental results demonstrate that when modular metastructures are prescribed a global shape/topology, the systems may yield significant and valuable properties adaptivity including variation in reaction force magnitude and direction, numerous globally stable topologies, and orders of magnitude change in stiffness. The influences of important parameters on tailoring the displacement range of coexistent metastable states are investigated to provide insight of how the assembly strategy governs the intriguing versatility and functionality which may be harnessed.

Keywords

Modular structure, metastructure, adaptive properties, shape change, muscle inspired

Introduction and motivation

Skeletal muscle is a remarkable, natural system combining adaptability, durability, robustness, and energetic versatility (Lindstedt et al., 2001; Lombardi et al., 1992; Shimamoto et al., 2009). These characteristics are desirable for engineered structural/material systems to achieve high performance, safety, and sustainability in many mechanical, aerospace, and civil applications (Gomez and Garcia, 2011; Kuder et al., 2013; Peraza-Hernandez et al., 2014). Recent study on a mechanical model, developed by Caruel et al. (2013), found that the nanoscale constituents of muscle, termed cross-bridges, are a critical source for muscle's intriguing passive, macroscopic functionalities once assembled into microscale assemblies called sarcomeres. These characteristics include means to "amplify interactions, ensure strong feedback, and achieve considerable robustness in front of random perturbations" (Caruel et al., 2013). In the mechanical representation, the cross-bridge was shown to exhibit coexistent *metastable* states for the same sarcomere length (Caruel et al., 2013; Marcucci and Truskinovsky, 2010). The metastable configurations represent the cross-bridge in either pre- or post-

power stroke during the sarcomere contraction cycle which is the origin of macroscopic force (Tortora and Derrickson, 2006). The study modeled the passive cross-bridge as bistable and linear springs in series (Caruel et al., 2013), thus identifying equivalent structural constituents that emulate the essential ingredients of muscle's manifestation of metastability.

Inspired by the intriguing versatility elucidated in the recent studies of cross-bridges and sarcomeres, the goal of this research is to develop and explore a new class of adaptive structures possessed with muscle-like versatility and multifunctionality. By the development and strategic assembly of mechanical *metastable modules*, this research examines a novel concept for engineering passive-adaptive *metastructures*. The term "metastable module" denotes that the module exhibits coexistent

Department of Mechanical Engineering, University of Michigan, Ann Arbor, MI, USA

Corresponding author:
RL Harne, Department of Mechanical Engineering, University of Michigan, Ann Arbor, MI 48109-2125, USA.
Email: rharne@umich.edu

metastable states for the same topology/shape—like the cross-bridge pre- and post-power stroke configurations for a prescribed sarcomere length. "Metastructure" denotes that the modular structural/material system is invested with unprecedented characteristics derived from a synergy of the assembled members. Through the biologically inspired constituent and assembly strategy, the aim is to uncover and elucidate the advanced functionalities and versatility invested in passive-adaptive engineered systems when a metastable building block is translated upwards from the nanoscale.

The following sections present analytical and experimental studies on the design and assembly of metastable modules into assembled metastructures. Investigations first illustrate the basic concept and uncover the single-module-level adaptivity generated due to coexisting metastable states. The studies then closely explore the opportunities produced in consequence to modular assembly for a dual-module metastructure. Analyses and experiments explore how tailoring individual module design parameters governs the adaptability features of the assembled metastructure, which gives insights on means to effectively guide module development to achieve desired metastructure versatility.

Mathematical formulation for metastable modules and assembled metastructures

In agreement with the previous cross-bridge model developed by Caruel et al. (2013), the one-dimensional, metastable modules created in this research are each composed using bistable and linear springs in series (Figure 1). The parallel assembly of modules is then the basis for the metastructures examined here, similar to the sarcomere composition of cross-bridges

A model is developed to explore the mechanical properties of metastable modules and assembled metastructures. A schematic of an assembled metastructure is shown in Figure 1. For this system, n modules are arranged in parallel with respect to a common global end displacement z. Within each module, a bistable spring with restoring force

$$F_{iB}(x_i) = k_{iB}x_i(x_i - a_i)(x_i - 2a_i) \tag{1}$$

is connected in series to a linear spring having restoring force $F_{iL} = k_{iL}(z - x_i)$. Here, x_i is the internal displacement representing the deformation of the bistable spring of the ith module from the static equilibrium $x_i = 0$; a_i is the ith bistable spring span which denotes the distance between the unstable and stable equilibrium positions of the bistable spring; and k_{iB} and k_{iL} are the stiffnesses. Note that the bistable spring force expression indicates there is a symmetry between the statically-stable equilibria of the bistable spring and the central unstable position (when disconnected from the
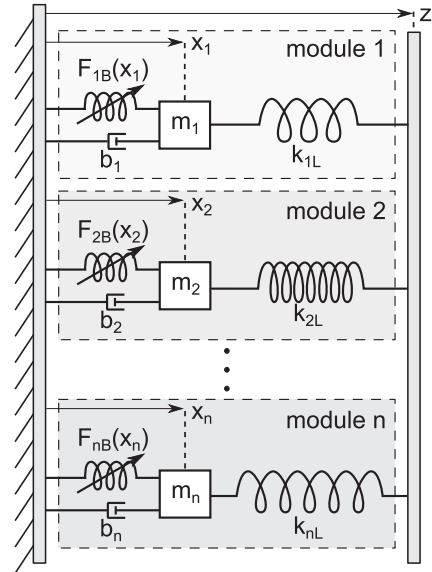

Figure 1. Schematic of the modular metastructure with n metastable modules assembled in parallel with respect to a common global end displacement z.

linear spring). In contrast to the previous model of the cross-bridge which utilized a bilinear/bistable spring (Caruel et al., 2013; Marcucci and Truskinovsky, 2010), the metastable module employs a continuous bistable spring characterized using a cubic polynomial for the spring restoring force to more accurately reflect the experimental bistable element behavior. The total potential energy of the metastructure is expressed by

$$U = \sum_{i=1}^{n}$$

$$\left[\frac{1}{2}(2a_i^2 k_{iB} + k_{iL})x_i^2 - a_i k_{iB}x_i^3 + \frac{1}{4}k_{iB}x_i^4 - k_{iL}zx_i + \frac{1}{2}k_{iL}z^2\right] \tag{2}$$

which is a function of internal coordinate positions x_i as well as the global end displacement z. A metastable internal state/configuration for a fixed global topology z of the metastructure satisfies $\partial U/\partial x_i = 0$ and $\partial^2 U/(\partial x_i \partial x_j) > 0$, where the latter indicates that the Hessian matrix is positive definite (Puglisi and Truskinovsky, 2000). The former constraint leads to a series of force balance equations, one for each module in the assembly

$$k_{iB}x_i^3 - 3a_i k_{iB}x_i^2 + (2a_i^2 k_{iB} + k_{iL})x_i$$
$$- k_{iL}z = 0; \quad \forall i = 1, 2, \ldots, n \tag{3}$$

The solutions to equation (3), that is, the roots of the cubic polynomials in terms of parameter x_i, are substituted into the Hessian matrix to evaluate for positive definiteness. Since the system is assembled from modules in parallel, the modules are statically decoupled for

prescribed end displacements z. Therefore, the determination of positive definiteness is equivalent to inspecting $\partial^2 U/\partial x_i^2 > 0 \quad \forall i = 1, 2, \ldots, n$. From equation (3), the cubic polynomial may have at most three stationary points, and at most two of them are stable via $\partial^2 U/\partial x_i^2 > 0$. Thus, for each module in the metastructure, there are at most two configurations satisfying both constraints. The two real roots of the ith cubic polynomial require that the respective discriminants of equation (3) satisfy

$$
\begin{aligned}
\Delta_i = {} & 54 k_{iB}^2 a_i k_{iL} (2a_i^2 k_{iB} + k_{iL}) z - 108 k_{iB}^3 a_i^3 k_{iL} z \\
& + 9 k_{iB}^2 a_i^2 (2a_i^2 k_{iB} + k_{iL})^2 \\
& - 4 k_i (2a_i^2 k_{iB} + k_{iL})^3 - 27 k_{iB}^2 k_{iL}^2 z^2 \geq 0
\end{aligned}
\tag{4}
$$

Equation (4) can be rearranged into a quadratic polynomial inequality in terms of global end displacement z

$$
C_{i2} z^2 + C_{i1} z + C_{i0} \leq 0
\tag{5}
$$

Here, the coefficients $C_{i2} = 27 k_{iL}^2 k_{iB}^2$, $C_{i1} = -54 a_i k_{iL}^2 k_{iB}^2$, and $C_{i0} = k_{iB}(4k_{iL} - a_i^2 k_{iB})(k_{iL} + 2a_i^2 k_{iB})$ are functions of spring stiffnesses and the bistable springs' spans a_i. Therefore, the end displacements leading to multiple coexistent metastable states for each module can be explicitly derived as a function of system parameters from equation (5) and satisfy the following criterion

$$
\frac{-C_{i1} - \sqrt{C_{i1}^2 - 4C_{i2}C_{i0}}}{2C_{i2}} \leq z \leq \frac{-C_{i1} + \sqrt{C_{i1}^2 - 4C_{i2}C_{i0}}}{2C_{i2}};
$$
$$
\forall i = 1, 2, \ldots, n
\tag{6}
$$

Consequently, the extent of the metastability range for a metastructure assembled from n modules is determined using

$$
\bigcup_{i=1}^{n} \left[\frac{-C_{i1} - \sqrt{C_{i1}^2 - 4C_{i2}C_{i0}}}{2C_{i2}}, \frac{-C_{i1} + \sqrt{C_{i1}^2 - 4C_{i2}C_{i0}}}{2C_{i2}} \right]
\tag{7}
$$

Having determined the metastable states of the metastructure, the total, static end (reaction) force for prescribed global topology z is found using $F_{end} = \sum_{i=1}^{n} k_{iL}(z - x_i)$. The stiffness of the metastructure at each global end displacement is obtained by Hooke's law

$$
k_a = \frac{\partial F_{end}}{\partial z} = \sum_{i=1}^{n} k_{iL} \left(1 - \frac{\partial x_i}{\partial z} \right)
\tag{8}
$$

where $\partial x_i/\partial z$ is determined implicitly from equation (3).

These static properties of metastable modules and assembled metastructures are then utilized in a dynamical model formulation for the case when the systems are acted upon by slow, periodic end displacements, such that the frequency of the excitation is significantly less than the linearized natural frequency of any given module. Inertial influences in the metastable modules are accounted for via including masses m_i that interface the bistable and linear springs. Additionally, damper elements are included in parallel with the bistable springs to take into account dissipative effects. Since the modules are assembled in parallel, the equations of motion for the internal masses m_i are decoupled under end displacement–controlled motions, leading to

$$
m_i \ddot{x}_i + b_i \dot{x}_i + F_{iB}(x_i) = k_{iL}(z - x_i); \quad \forall i = 1, 2, \ldots, n
\tag{9}
$$

with $F_{iB}(x_i)$ defined in equation (1). Based on a prescribed, periodic end displacement $z(t)$, the instantaneous total end force is then

$$
F_{end}(t) = \sum_{i=1}^{n} k_{iL}(z(t) - x_i(t))
\tag{10}
$$

In this study, the area enclosed in hysteresis loops induced in consequence to the periodic end displacement actuations is used to evaluate the energy dissipation capacity of modules and metastructures

$$
E = \int_{z(0)}^{z(T)} F_{end}(t) \, dz(t)
\tag{11}
$$

where T is the end displacement excitation period.

Properties of a proof-of-concept cross-bridge inspired metastable module

Mechanical properties

To illustrate the adaptable mechanical properties of the metastable module similar to the characteristics of the coexisting pre- and post-power stroke states of muscle's cross-bridge constituent, the following study examines a single module. For analytical insight, the model developed in the previous section is employed using the parameters $k_{1B} = 1 \, \text{N/m}^3$, $a_1 = 1 \, \text{m}$, and $k_{1L} = 0.3 \, \text{N/m}$ across a range of static end displacements. The parameters are arbitrarily selected, at this stage in development, for qualitative comparison between analytical predictions and experimental findings. Figure 2(a) presents the potential energy profile of the individual module as the end displacement varies. Throughout this work, in the profiling of potential energy, force, and stiffness as end displacement is varied, the distinct line styles represent the mechanical properties due to different combinations of metastable internal configurations and thus are representative of the different metastable states. The results in Figure 2(a) show clearly that coexisting metastable states are induced across a certain range of end displacement values. In the figure, these displacements
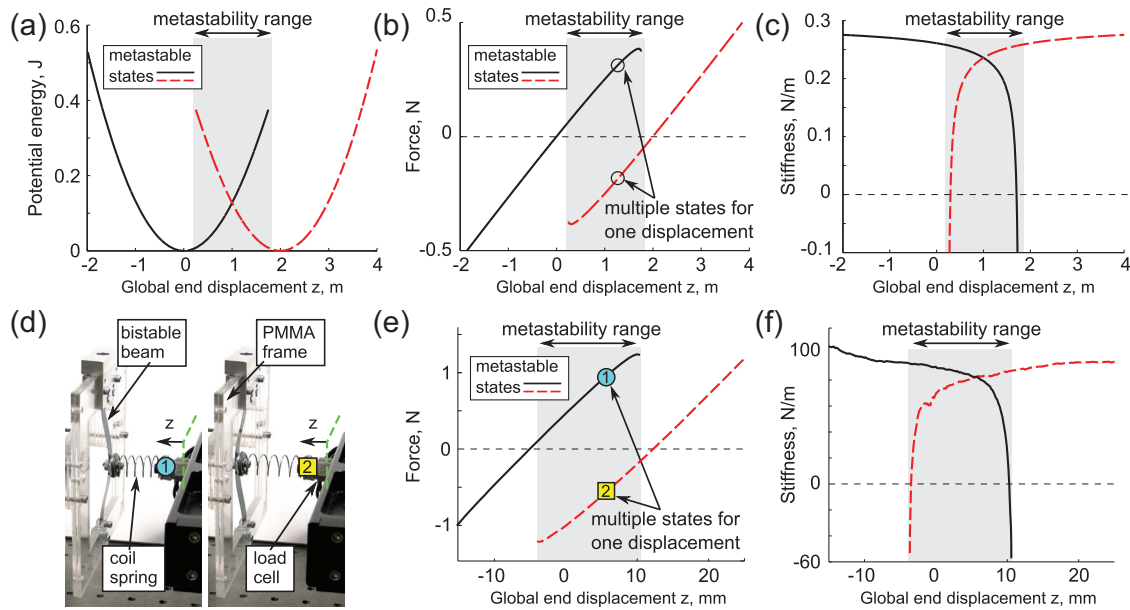
Figure 2. Single-module analytical results of (a) potential energy, (b) reaction force, and (c) stiffness as functions of global displacement. (d) Single-module experimental setup and measurements of (e) reaction force and (f) stiffness. Markers regarding coexistent forces/displacements in (e) correspond to coexistent metastable configurations in (d). Light shading denotes metastability range where structural adaptation is realized, and each line indicates a metastable state.

are denoted as the *metastability range*, defined as the range of global displacements *z* within which multiple metastable configurations coexist, and are featured in Figure 2 using the light background shading. For some prescribed end displacements, the coexistent metastable states exhibit *different* values of potential energy. The distinct potential energy values are of particular interest since this is the mechanism by which cross-bridges in sarcomeres achieve such remarkable characteristics as the efficient switching back-and-forth between pre- and post-power stroke states (Caruel et al., 2013). Indeed, recent studies on adaptive machines (Allahverdyan and Wang, 2013), metamaterials (Klatt and Haberman, 2013; Nicolaou and Motter, 2012), and sensory adaptation systems (Lan et al., 2012) provide complementary evidence that adaptive or non-natural characteristics may be induced when non-unique potential energies satisfy shared external constraints. Comparable, intriguing potential energy landscapes produced due to coexisting metastable states in a parallel "bundle of bistable snap-springs" have recently been shown by Caruel et al. (2015) to be distinct with respect to *displacement*-controlled and *force*-controlled loading scenarios representative of isometric and isotonic loading, respectively, on skeletal muscle networks. Yet, in spite of the differences, it was shown that coexisting metastable states are observed in both loading scenarios (Caruel et al., 2015). As a result, to focus the attention of this research on the properties *adaptation* enabled by *leveraging* the coexisting metastable states, the following studies consider the case of displacement-controlled loading for insights obtained through a channeled and systematic exploration.

For the following experimental explorations and studies, proof-of-concept metastable modules are fabricated using frame-mounted bistable springs, realized using compressed and buckled spring steel beams fixed into supporting poly(methyl methacrylate) (PMMA) frames. The bistable springs are then connected in series to a linear compression coil spring, aligned to translate uniaxially (Figure 2(d)). The coil spring is attached to the center point of the buckled beam and is acted upon by prescribed global topologies/displacements *z* on the opposing end. For experimentation with a single module, the opposing coil spring end is attached to a load cell which is attached to a quasi-statically actuated electrodynamic shaker. The shaker displacement (the global topology/displacement *z*) is measured using a laser interferometer. Stiffness is determined by the derivative of the force–displacement profiles. The supporting frames measure 0.15 m × 0.15 m × 6.5 mm with an interior cavity of 0.1 m × 0.1 m. Thus, 0.1 m is the spring steel beam length prior to applying axial compression to buckle the beam. The spring steel beams are 0.127 m wide × 0.18 mm thick. Axial beam compression is accomplished via micrometer adjustments against a sliding end of the beam clamping fixture inside the frame. The straightforward design of the fabricated metastable modules captures the essential, passive mechanical ingredients of the cross-bridge and, indeed, is advantageous so that investigations can be focused on the new phenomenological behavior without potential misdirection by nonessential elements. In Figure 2(d), the physical configurations of two coexistent metastable states are illustrated for the

experimental system, showing that for one prescribed global end displacement z, the internal state (coordinate) x may rest at one of two metastable configurations. Such coexistence of metastable states for a single module is the key feature derived from the cross-bridge inspiration.

Due to the non-uniqueness in the potential energy, the metastable module exhibits adaptivity in the mechanical properties across the metastability range. The analytical and experimental results (Figure 2(b) and (e), respectively) reveal multiple static equilibria topologies, indicated by the global displacements satisfying zero force. Moreover, the results in Figure 2(b) and (e) show that magnitude and direction adaptation of module reaction forces is possible via switching between coexistent metastable states for certain fixed values of end displacement. The connections between metastable state realization and corresponding reaction force behaviors are exemplified experimentally by the markers labeled 1 and 2 in Figure 2(d) and (e).

In fact, a large body of research has considered exploiting the stable configurations of bistable structures for adaptivity and functionality enhancements. Among many recent examples, Johnson et al. (2013) investigated energy dissipation of a bistable oscillator showing drastic passive-adaptive power dissipation capability depending on the harmonic excitation characteristics. Pontecorvo et al. (2013) examined the bistable behavior of an arch for morphing applications and provided detailed design guidelines to exploit bistability for shape change and load support. Schultz (2008) investigated a new concept of bistable twisting plates for adaptive airfoil morphing enabled by the strategic fabrication of composite laminates. Inspired by a folding mechanism observed in nature, Daynes et al. (2014) developed an elastomeric bistable cell geometry capable of reversibly unfolding from a flat configuration to a highly textured configuration which could potentially be used as a means of adaptive camouflage. Wu et al. (2015) elucidated the parameter sensitivities of harmonically excited bistable structures to selectively achieve desired dynamic displacement amplitudes and mean response values, which serve as operating guidelines for a wide range of applications that strategically utilize several of the dynamic behaviors. These possibilities for adaptivity enhancements are due to the nature of the force–displacement profiles for bistable structures which are bi-valued in displacement for the same force (Kovacic and Brennan, 2011). Yet, in great contrast, the unique adaptability of reaction force for a fixed global topology is *only* possible owing to the fact that the metastable module is not only bi-valued in displacement for constant force but also bi-valued in force for the same global end displacement. Thus, even though the metastable module includes a bistable element, the capacity for multiple coexistent metastable states sharply differentiates the metastable module from a strictly bistable system. In fact, the metastable module is more analogous to a *phase-transition material* since the shape remains constant while its reaction to the environment drastically alters via change between coexistent metastable states.

In addition to adaptation of the reaction force, by Hooke's law the metastable module may exhibit one of two stiffnesses corresponding to the respective metastable states. Between these two states, orders of magnitude in stiffness variation may be observed experimentally and analytically (Figure 2(e) and (f)). The global topologies for which stiffness adaptations are most dramatic are seen to occur near the extremes for which the respective metastable configurations occur. For example, measurements reveal more than four orders of magnitude stiffness change by switching between metastable configurations when the global displacement is fixed at $z = 10$ mm (86.71 N/m to 0.02799 N/m), Figure 2(f). Moreover, the analytical and experimental results find that the module may realize negative stiffness at the extremities of the metastability range (Figure 2(e) and (f)). Due to the global end displacement constraint for the module, it has been shown that negative stiffness may in fact be "stabilized" (Lakes and Drugan, 2002).

Energy dissipation for low-frequency dynamic excitation

A dynamic study using the model of a single metastable module is conducted to examine how the significant adaptation in the mechanical properties is translated to energy dissipation characteristics. In addition to the previous module parameters, this dynamic study employs values of internal mass $m_1 = 1$ kg and damper constant $b_1 = 0.5$ N/(m/s). The global end displacement z is prescribed to be a triangular wave with peak-to-peak amplitude A = 5 m and period $T = 2 \times 10^4$ s, as shown in Figure 3(a), and the displacement begins at one of the statically-stable equilibrium, marked by the circle in Figure 3(b). The prescribed dynamic end displacement is such that it encompasses the full range of static end displacements considered in Figure 2. From numerically integrating equation (9) under these conditions, the instantaneous reaction force, computed using equation (10), is depicted in Figure 3(b) with arrows indicating the trajectory of the force over time. As shown in Figure 3(b), when the global end displacement approaches the extremes of the metastability range, sudden dramatic changes in both force level and direction are observed due to the change in the internal configuration from one metastable state to the other. Such phase transition-like phenomena can lead to large hysteresis. Since the area of the hysteresis loop corresponds to energy dissipation over the course of an actuation cycle (Lakes, 2009), it is found that for this particular module design, the energy dissipation is
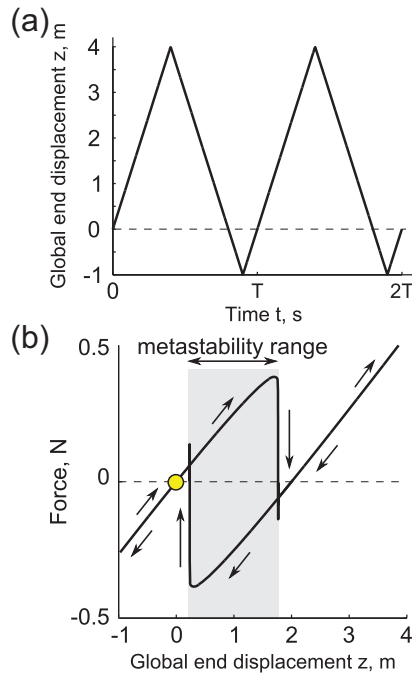
Figure 3. (a) Prescribed displacement profile for dynamic simulations. (b) Single-module analytical result of reaction force change as global displacement is slowly and continuously varied, with circle marker indicating the starting and final states. Arrows indicate direction of changes induced via the controlled change in end displacement.

0.73 J, according to equation (11). Although this energy dissipation mechanism is not a particular property exploited by cross-bridges in muscle (Caruel et al., 2013), leveraging sudden switches among metastable states in the metastable modules created and explored in this research is a novel approach to damping enabled as a result of the biologically inspired design. In fact, for material systems, similar means to achieve large damping has also been explored when the composites are composed of negative stiffness inclusions within positive stiffness elastic matrices, creating a material system that features metastable states for certain values of temperature (Lakes et al., 2001).

Analytical and experimental case studies of a dual-module metastructure

To explore how the intriguing mechanical and dynamical properties adaptivity of the metastable modules is transformed when modules are assembled together, this section investigates a dual-module metastructure for first insights.

Analytical case study for a dual-module metastructure

To begin, an analytical study of a dual-module metastructure is undertaken where the two modules are
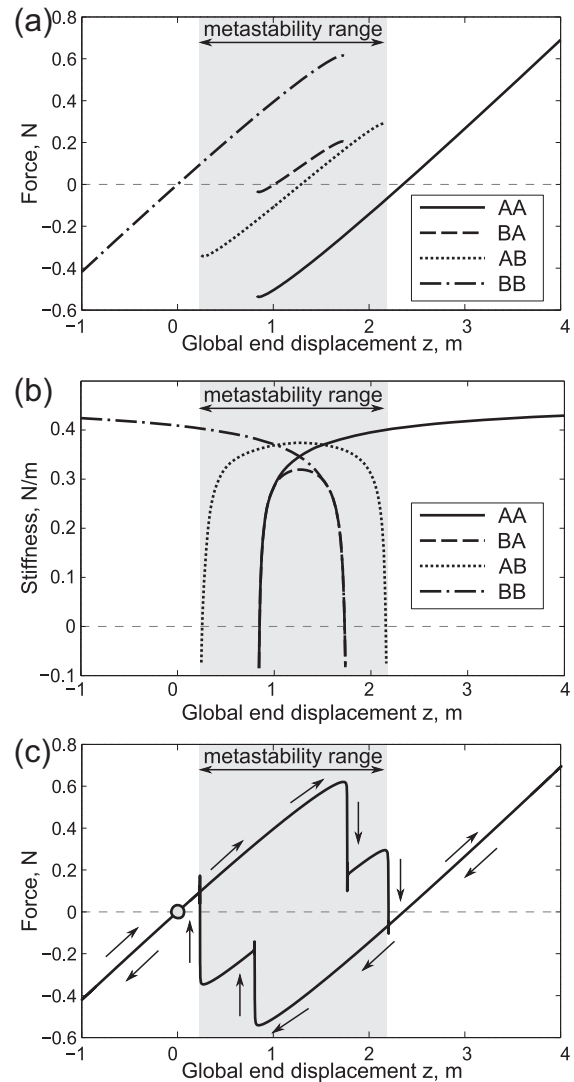

Figure 4. Analytical profiles for dual-module metastructure as global end displacement is varied: (a) end force and (b) stiffness. Different line styles denote different metastable configurations. (c) Reaction force change as global displacement is slowly and continuously varied, with circle marker indicating the starting and final states. Arrows indicate direction of changes induced via the controlled change in end displacement.

different in design, and hence in structural features. The specific parameters used in the analysis are $k_{1B} = 1\,\text{N/m}^3$, $a_1 = 1\,\text{m}$, $k_{1L} = 0.3\,\text{N/m}$, and $k_{2B} = 16/81\,\text{N/m}^3$, $a_2 = 3/2\,\text{m}$, and $k_{2L} = 8/45\,\text{N/m}$. The parameter values indicate that the stable equilibria of the two bistable springs of the modules are located at (0, 2) m and (0, 3) m, respectively. The parameters are chosen arbitrarily and are thus used for representative purposes in deriving first insights pertaining to the primary features of the metastructures. The global end forces and stiffnesses, as computed by the analytical model, are plotted in Figure 4. Here, the label AA indicates that the attachments between linear and bistable springs of both modules remain at positions with

displacements greater than the unstable static equilibria, that is, in this case study satisfying $x_1 > 1$ m and $x_2 > 1.5$ m, respectively. Conversely, the label BB means that these spring connections remain at positions with displacements less than the unstable static equilibria, and thus satisfy $x_1 < 1$ m and $x_2 < 1.5$ m, respectively. The mixed labels AB and BA denote the corresponding mixed cases of internal module configurations.

Figure 4(a) shows that the dual-module metastructure exhibits multiple distinct force profiles, one representing each metastable configuration set of the system. The plot also reveals four global displacements yielding zero reaction force which are statically-stable equilibrium positions. As shown in Figure 4, for this representative case, the metastability range spans from approximately $z = 0.25$ m to $z = 2.17$ m. As shown in the force profile, Figure 4(a), when the end displacement z is prescribed, at most four different reaction forces can be realized for this metastructure. In other words, the total number of coexisting metastable states multiplies from two to four as the two modules are assembled together. According to the model, by the parallel assembly of the metastable modules acted upon by end displacement constraints, the number of total possible coexisting metastable states is 2^n for an n-module metastructure, plainly a synergistic product of the metastructure development. In addition to changes in reaction force, by Hooke's law, Figure 4(b) shows that the dual-module metastructure exhibits large adaptability in stiffness when the global shape/displacement is held constant. In fact, orders of magnitude of stiffness variation may be achieved by switching among the internal states when global end displacement is fixed, for example, at $z \approx 1.7$ m. The large adaptation of stiffness afforded by the metastable module is an attractive capability to leverage for advancing structural functionality such as for shape morphing (Shan et al., 2009), wave-guiding (Fok et al., 2008), and vibration control (Bonello et al., 2005), just to name a few applications.

Similar to the dynamic study of the single metastable module, Figure 4(c) presents the instantaneous reaction force profile of the dual-module metastructure when it is acted upon by the slow, periodic end displacement excitation shown in Figure 3(a). The numerical integration of the equation system (9) for this metastructure employs the additional system parameters $m_1 = m_2 = 1$ kg and $b_1 = b_2 = 0.5$ N/(m/s). The circle point in Figure 4(c) denotes the starting position while the arrows indicate the instantaneous trajectory of reaction force. As shown in Figure 4(c), the sudden change in force amplitude occurs not only at the extremes of the metastability range, similar to the individual metastable module, but also occurs inside the metastability range. Each sudden transition in the force amplitude qualitatively corresponds to a change in internal metastable configuration. For this case, the energy loss per cycle is determined to be 1.27 J. In
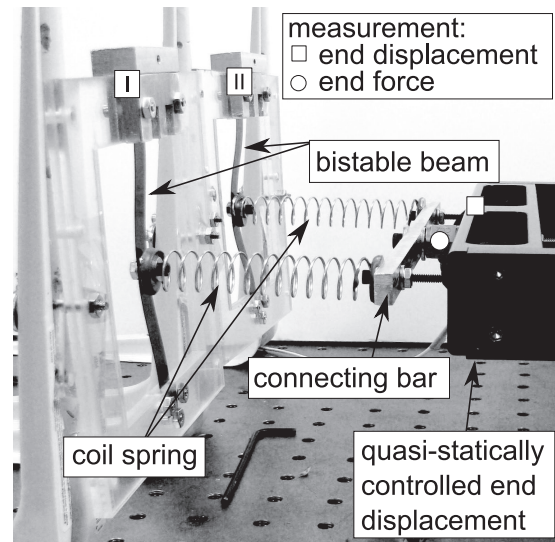

Figure 5. Photograph of a dual-module metastructure.

other words, by the assembly of two different metastable modules, the net energy dissipation capacity of the metastructure is increased by more than 70%. The more intricate features of how energy dissipation properties scale and are modulated by the modular assembly will be the focus of future research efforts.

Experimental case study for a dual-module metastructure

Following the analytical case study, the proof-of-concept experimental system is employed to verify the primary trends of the analysis regarding the mechanical characteristics empowered by assembling two metastable modules together to form a metastructure. Figure 5 shows the experimental setup of a dual-module metastructure, where the modules are labeled I and II. To realize the parallel assembly strategy, the other ends of the coil springs of each module are attached to a common rigid connecting bar that is connected to the controlled electrodynamic shaker to prescribe uniaxial motions. To evaluate all possible coexisting metastable states (if they occur for a given system design), the experiments are conducted to reconstruct the profiles satisfying the conditions that: (AA) both modules' bistable beam displacements remain to the right of the unstable equilibrium positions with respect to a central, vertical, pre-buckled configuration; (BB) both bistable beam displacements remain to the left, as shown in Figure 5; (AB) the bistable spring displacement of module I remains right and that of module II remains left; and (BA) the bistable spring displacement of module I remains left and that of module II remains right.

Figure 6(a) presents the measured force profiles of a dual-module metastructure as end displacement varies. In agreement with the trends predicted analytically in
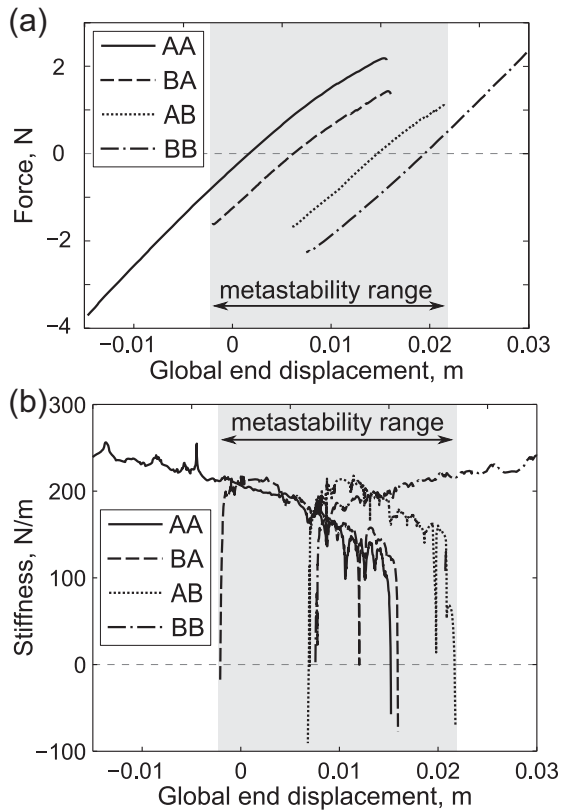
Figure 6. (a) Force and (b) corresponding stiffness profiles of the dual-module metastructure as global end displacement is varied.

Figure 7. (a) Force profiles of the dual-module metastructure as end displacement is varied. Circle points indicate statically stable topologies, correspondingly labeled as (1)–(4). (b) Time history of global end displacement as metastable configuration is changed to induce changes in global topology.

Figure 4(a), the measurements shown in Figure 6(a) reveal four distinct force profiles depending on the metastable configurations exhibited within the metastructure. In this case, each profile exhibits one global topology/displacement satisfying zero reaction force; thus, each metastable configuration set provides for a different statically-stable global topology. The measurements show that when the metastructure is prescribed a global displacement, switching among internal configurations may change amplitude and direction of the reaction force, which is also in agreement with analytical predictions. In addition, the experimental results in Figure 6(b) show that extreme change in stiffness may be realized by switching among the metastable configurations while the global end displacement is fixed, notably when the end displacement is held near the limits of stability for a given metastable state. Collectively, the results of Figure 6(a) and (b) verify the primary trends of the analysis and clearly demonstrate that the metastructures can yield dramatic mechanical properties adaptivity for constant global topology and induce a multiplying number of statically-stable equilibria across a broad metastability range of global displacement.

The analytical and experimental results suggest that switches among the metastable states provide
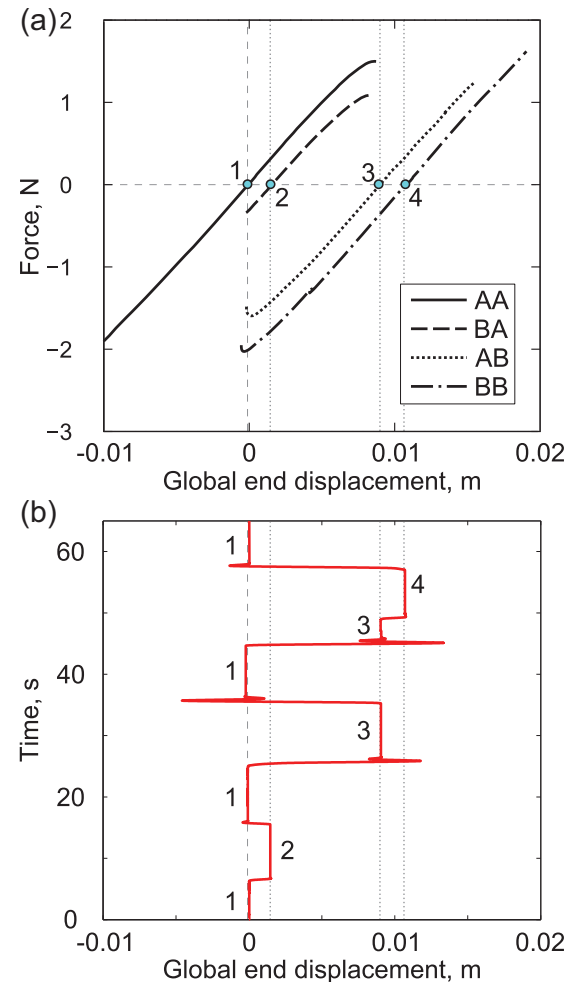
immediately reversible properties or change in global metastructure shape. To experimentally explore the reversible topology changes using metastable state switching, another dual-module metastructure is examined using dynamic transitions among the metastable configurations. First, Figure 7(a) plots the force profiles of the system, once again uncovering the characteristic multitude of unique mechanical properties which may be realized depending on the metastable configuration set of the assembled modules. The four statically-stable equilibria are labeled 1–4 in Figure 7(a) and highlighted via the circle points. Then, Figure 7(b) presents the time history of the global end displacement while the various metastable configurations are changed via fast manual actuations upon the attachments between module bistable and linear springs. In the experiment, the global end displacement is free to move according to its one-dimensional axis of motion as guided by an unconstrained motion of the shaker upon
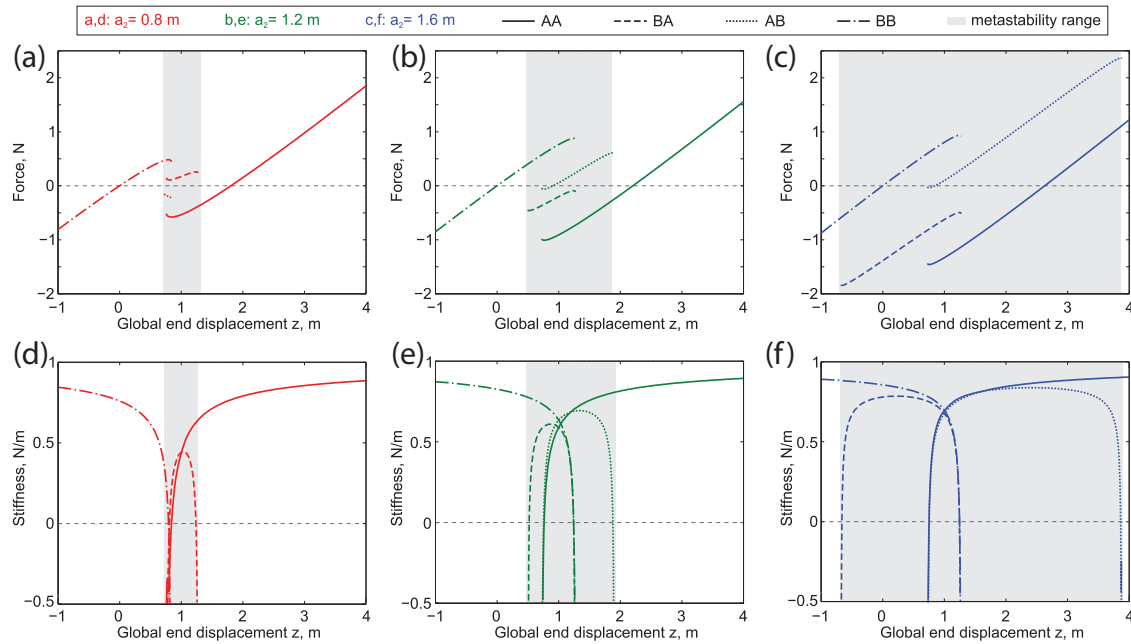
Figure 8. Profiles of (a, b, c) end force and (d, e, f) stiffness as global end displacement is varied for the dual-module metastructure. From left to right for both rows, the bistable spring span a_2 of the second module increases.

the low-friction shaker guide rails. Both modules start at positions to the right of the unstable equilibria of the bistable beams (AA) with respect to the pre-buckled configurations, such that the initial global displacement is the statically stable topology labeled 1 in Figure 7(a). By switching the internal coordinate of module I to the left of the bistable beam unstable equilibrium, realizing the BA configuration, the global end position immediately changes to the topology labeled 2, which is another statically stable metastructure topology, as shown in Figure 7(a). The corresponding time history of global displacement at the point of the metastable state switch is shown in Figure 7(b) at time around 6 s, and the reversible switch back to topology 1 occurs around time 15 s. This process is repeated for the changes in topology 1 to 3 to 1, and 1 to 3 to 4 to 1. The experimental demonstration of metastable state transitions verifies the reversibility of switching among the metastable configuration sets as means to realize repeatable and consistent changes in statically-stable global topologies. Likewise, reversible adaptation in force amplitude, and potentially force direction, can be achieved within the metastability range by switching among internal configurations when global end displacement z is fixed. Moreover, according to the analytical model, the number of potential coexisting metastable states increases exponentially, a finding from which one could hypothesize empowers a significant opportunity for reversible properties adaptivity due to the assembly of many modules in the metastructure.

Parametric study for a dual-module metastructure

The unique adaptations in shape and mechanical properties observed from the case studies of the previous sections illustrate that the metastructures may provide high potential for engineering applications in which such versatility is advantageous, including morphing aircraft (Barbarino et al., 2011), energy absorption (Tolman et al., 2014), and load impedance control (Philen, 2009), to name a few. To develop an understanding of how to take the greatest advantage of these features, the sensitivities of metastructure properties are evaluated as key design parameters are changed. In this research, except the number of modules in the parallel assembly, all the design parameters are at the module level. In the following sections, as individual metastable module design parameters are varied, the changes in overall metastructure characteristics are examined.

Analytical study of change in bistable spring span a_2

In this section, the analytical model is employed to investigate the influence on metastructure properties due to changing span between the statically-stable equilibria of the bistable spring of the second module, denoted by parameter a_2. The other system parameters for the following study are $k_{1B} = k_{2B} = 1\,\mathrm{N/m^3}$, $k_{1L} = k_{2L} = 0.5\,\mathrm{N/m}$, $a_1 = 1\,\mathrm{m}$, and $a_2 = [0.8, 1.2, 1.6]\,\mathrm{m}$. The top row of Figure 8 plots the global end force as a function of global displacement, while the

bottom row of Figure 8 depicts the corresponding stiffness profiles. The labeling convention for the metastable configurations is the same as employed in the case studies. From left to right, the bistable spring span a_2 increases from 0.8 to 1.2 to 1.6 m.

As clearly shown in Figure 8, the metastability range increases as the bistable spring span a_2 increases. This is due to the fact that as the bistable spring span of the second module increases, according to equation (1) the corresponding peak force amplitudes of the second module bistable spring are increased at the displacements that transition from positive to negative stiffness values (for reference, the feature here discussed is explicitly observable in Figure 10 in the following experimental studies). This in turn makes it possible to stabilize the metastable states over progressively increasing ranges of global displacement because larger forces are required to deform the linear spring (and hence extend the range of end displacement) in order to counterbalance the increasing bistable spring forces.

As shown in Figure 8(d) to (f), it is observed that the change in bistable spring span a_2 has little effect on the stiffness profiles at very small and large displacements of the dual-module metastructure. On the other hand, increases in the second module bistable spring span parameter are seen to gradually increase the location at which the static equilibrium position of the AA metastable configuration occurs. Finally, it is observed that as the bistable spring span a_2 increases, considering the columns of Figure 8 from left to right, the ranges of displacements over which the metastable configurations AB and BA occur also increase. This effect is especially prominent for configuration AB, where the range is almost non-existent considering the case of shortest bistable spring span (Figure 8(a) and (d)), yet is found to extend over a majority of the total metastability range for the largest bistable spring span (Figure 8(c) and (f)). The latter finding is important because each metastable state provides for a unique force and stiffness profile, which the metastructure may favorably harness for adaptation of the mechanical properties. Thus, a wider range of displacements across which each unique metastable configuration profile exists provide for a broader range of global topologies that are empowered with advantageous adaptivity.

The previous sections found that dynamic end displacements may trigger sudden changes in the internal metastable configuration set of the metastructure which leads to large periodic hysteresis and hence energy dissipation. To investigate the influence of the bistable spring span a_2 on the energy dissipation capacity, the dynamic model of the dual-module metastructure is numerically integrated for the case that the end displacement is periodically actuated in the style shown in Figure 3(a); the remaining system parameters for the slow dynamic model evaluation are $m_1 = m_2 = 1\,\text{kg}$ and $b_1 = b_2 = 0.5\,\text{N}/(\text{m}/\text{s})$. Following equation (11),

the energy dissipation per cycle of the metastructure increases from 0.42 to 1.70 to 6.65 J as the bistable spring span a_2 increases. Such significant increase in energy dissipation per actuation cycle (more than an order of magnitude) serves as further evidence of the extreme adaptability of metastructures composed from the metastable modules.

Analytical study of change in linear spring stiffness k_{2L}

The analytical model is utilized to explore how characteristics of the dual-module assembly are influenced due to changes in linear spring stiffness k_{2L}. The parameters for the study are $k_{1B} = k_{2B} = 1\,\text{N}/\text{m}^3$, $k_{1L} = 0.5\,\text{N}/\text{m}$, $a_1 = 1\,\text{m}$, $a_2 = 1.25\,\text{m}$, and $k_{2L} = [0.4, 0.8, 1.2]\,\text{N}/\text{m}$. Similar to the plotting convention in Figure 8, the top row of Figure 9 presents the end force profiles while the bottom row shows the corresponding stiffness profiles for the dual-module metastructure. In both rows of Figure 9 from the left-most column to the right-most column, the linear spring stiffness k_{2L} increases from 0.4 to 0.8 to 1.2 N/m. As shown in Figure 9(a) to (c), for the range of the linear spring stiffnesses k_{2L} employed in this parametric study, all three cases preserve the characteristic four distinct force profile paths per dual-module assembly. Two primary trends are observed for increasing values of linear spring stiffness k_{2L}. First, the metastructure stiffnesses for very small or very large end displacements are seen to increase (Figure 9(d) to (f)); this is in sharp contrast to the observations in the prior section that metastructure stiffness variation is negligibly influenced for the extreme end displacements as bistable spring span is changed. Yet, for displacements within the metastability range, the trends of global stiffness change are more intricate as linear spring stiffness is tailored. For example, as the linear spring stiffness k_{2L} increases, the metastable configurations labeled as AB exhibit broader ranges of end displacement having negative or very small positive stiffness values, as shown in Figure 9(d) to (f) by considering the plots from left to right. These trends may be explained by considering that the upper bound in effective stiffness of two springs in series is determined by the weaker link. Therefore, as the linear spring stiffness k_{2L} increases, the "negative stiffness" characteristic of the bistable spring constituent has greater influence on the module-level stiffness profiles, which is reflected in the profile for the dual-module metastructure.

The second primary trend is that the metastability range decreases as linear spring stiffness k_{2L} increases. This finding is intuitive when one considers the limiting case in which the linear spring k_{2L} becomes nearly rigid. In this situation, the global end displacement is effectively connected directly to the bistable spring internal coordinate of the second module. Consequently, the
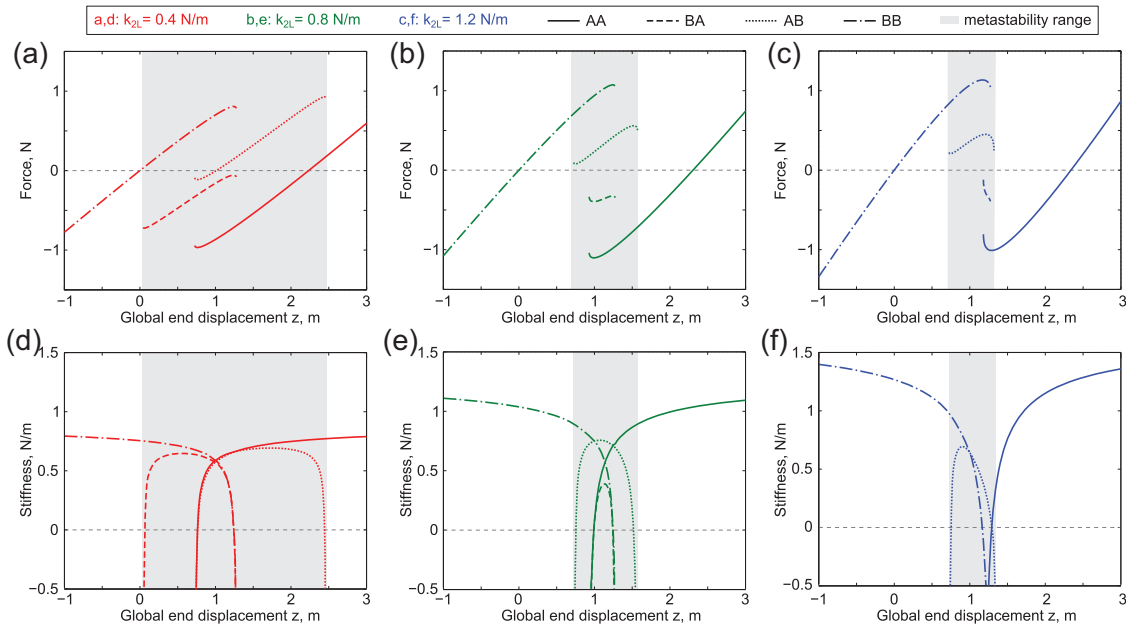
Figure 9. Profiles of (a, b, c) end force and (d, e, f) stiffness as global end displacement is varied for the dual-module metastructure. From left to right for both rows, the linear spring stiffness k_{2L} increases.

metastability range for the second module will be 0, although there is still the possibility of a finite metastability range of the dual-module metastructure but this depends on the design parameters of the first module according to equation (7).

Again using the dynamic model of the dual-module metastructure, the energy dissipation per cycle due to slow actuations of the metastructure is seen to decrease from 2.37 to 1.25 to 0.60 J as linear spring stiffness increases. Since the previous dynamic modeling results found that large hysteresis is a consequence of a large metastability range, the reduction in the metastability range due to the increase in the linear spring stiffness plainly reduces the potential for considerable energy dissipation.

Experimental parametric study

An experimental dual-module metastructure is employed to examine the influences of changing the parameters that were investigated in the prior sections: the linear spring stiffness and bistable spring span of one of the modules. The experimental studies are intended to verify the primary analytical observations as well as to gather meaningful insight about practical factors involved in assembling metastructures from the current proof-of-concept modules.

To begin, a series of experiments are conducted by varying the bistable spring span of module II while all other parameters of the metastructure remain constant. The span is changed by adjusting the compression distance on the buckled beam in module II. The measured force profiles for the four cases of bistable springs used
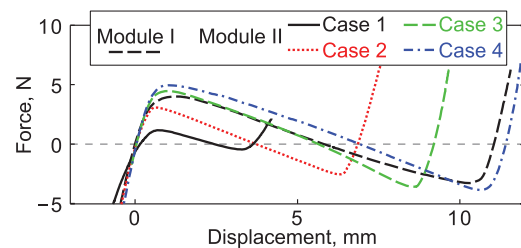

Figure 10. Force profiles of the bistable springs of modules I and II as the bistable spring displacement is varied. The dashed curve corresponds to the bistable spring force profile for module I, whereas the remaining curves are those employed for module II. The spans of the bistable springs used for module II increase from 1 to 4 as labeled in the plot.

bistable in module II are presented in Figure 10, showing that from case 1 to case 4, the span gradually increases. Due to the slight asymmetry observed in the force–displacement profiles (Figure 10), the experimentally determined bistable spring span is quantified as the average of the two distances from each respective stable equilibria to the central unstable equilibrium. For completeness, Figure 10 also shows the relation of the spring span for module I. In addition, note the feature that the peak force amplitude gradually increases as the static equilibria span of the bistable spring of module II is increased, as discussed in the analytical parametric study.

In Figure 11, the end force (top row) and stiffness (bottom row) profiles of the dual-module metastructure are presented for all four cases of bistable spring span, as it is gradually increased from case 1 to case 4
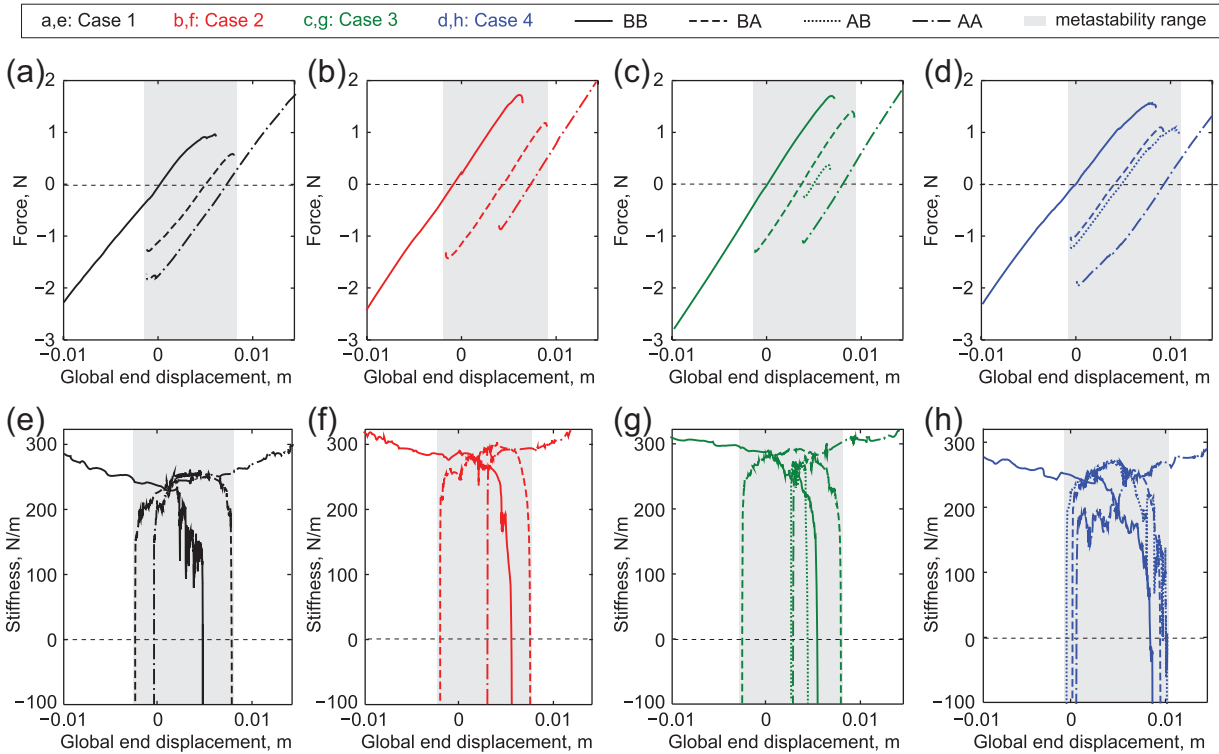
Figure 11. Measured profiles of (a, b, c, d) end force and (d, e, f, h) stiffness as global end displacement is varied for the dual-module metastructure. From left to right for both rows, the bistable spring span of module II increases from example 1 (far left) to example 4 (far right).

considering the figure columns from left to right. In agreement with the analytical trends shown in Figure 8, it is experimentally observed that as the bistable spring span of module II increases from cases 1 to 4, the range of existence for the metastable configuration AB noticeably increases. Due to the current experimental constraints that measurements begin from a statically-stable (zero force) position for each combination of internal configurations, the total absence of the AB configuration force profiles in Figure 11(a) and (b) may be caused by the fact that these force profiles do not include a statically-stable (zero force) position and therefore could not be identified experimentally, rather than the fact that the entire AB metastable configuration does not exist. Yet considering Figure 11 further, also in agreement with analytical findings, it is found that the change in bistable spring span does not appreciably affect the stiffness of the metastructure for very small or very large end displacements, as seen in Figure 11(e) to (h): the maximum stiffness for such displacements remains around 300 N/m for all cases. However, the increase in the bistable spring span is observed to shift the location of the statically-stable equilibrium of configuration AA to higher values of displacement, from approximately 7.5 to 10 mm as shown in Figure 11. Each of these findings is in very good agreement with the observations from the analytical parametric study by employing the mathematical model.
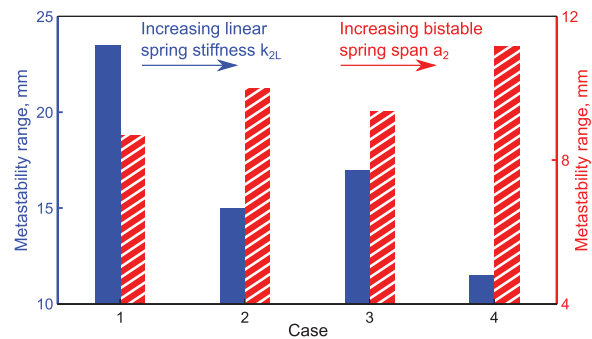

Figure 12. Metastability range as linear coil spring stiffness (solid/blue and left-most vertical axis measures) and bistable spring span (dashed/red and right-most vertical axis measures) varies.

The experiments are then performed to investigate the influence of changing the linear spring stiffness of module II using the coil spring stiffnesses of 54, 77, 98, and 122 N/m, denoted here as cases 1–4, respectively, while all other metastructure parameters remain the same. For comparison, the linear spring stiffness of module I is 122 N/m throughout the following evaluations. Figure 12 quantifies the trends observed in the measurements on how the metastability range of the dual-module metastructure is affected as linear coil spring stiffness (solid bars/blue) and bistable spring span (dashed bars/red) of module II are varied. Cases

1–4 correspond to either increase in linear coil spring stiffness or increase in bistable spring span, where the latter results were considered in full detail via Figure 11. As depicted in Figure 12, the general trend is that the metastability range of a dual-module metastructure increases as the linear spring stiffness decreases or as the bistable spring span increases. These findings are in accord with the analytical observations described in the analytical and experimental parametric studies and examined in Figures 8 and 9. To maximally harness the mechanical properties adaptivity of the metastructure, a multitude of coexistent metastable states must be realized over a broad range of end displacements. The results of the parametric studies indicate that the linear spring stiffness and the span between bistable spring static equilibria are critical toward governing the breadth of the metastability range. Moreover, the findings indicate that even one module of a multi-module assembly may play a lead role in determining the metastructure properties by the adjustment of a single-module-level constituent.

Conclusion

To achieve significant adaptivity and multifunctionality in engineered structures, this research explored a new concept to create engineered metastructures from the assembly of mechanical, metastable modules. The idea is inspired by recent mechanical study of the micro- and nanoscale composition of skeletal muscle, which gave evidence that the nanoscale, metastable cross-bridge constituents and their assembly are a critical source of the intriguing and favorable properties adaptivity evident in muscle on the macroscale. The critical features of the modular platform are the exploitation of multiple coexistent metastable states engendered via the strategic module design, and the adaptable properties that are produced in consequence to switching among states. Through analysis and experimentation, it is found that metastructures are endowed with immediately reversible adaptation of global shape/topology and the mechanical properties. By the theoretical development, the potential for adaptivity is seen to grow synergistically according to the increasing number of assembled modules. The versatile characteristics include orders of magnitude stiffness change, variable reaction force amplitude and direction, and tunable energy dissipation capacity. Analytical and experimental parametric studies show that the design parameters of linear spring stiffness and bistable spring span of even one module may play a key role toward influencing the modular metastructure global properties adaptivity.

Declaration of Conflicting Interests

The authors declared no potential conflicts of interest with respect to the research, authorship, and/or publication of this article.

References

Allahverdyan AE and Wang QA (2013) Adaptive machine and its thermodynamic costs. *Physical Review E* 87: 032139.

Barbarino S, Bilgen O, Ajaj RM, et al. (2011) A review of morphing aircraft. *Journal of Intelligent Material Systems and Structures* 22: 823–877.

Bonello P, Brennan MJ and Elliott SJ (2005) Vibration control using an adaptive tuned vibration absorber with a variable curvature stiffness element. *Smart Materials and Structures* 14: 1055.

Caruel M, Allain JM and Truskinovsky L (2013) Muscle as a metamaterial operating near a critical point. *Physical Review Letters* 110: 248103.

Caruel M, Allain JM and Truskinovsky L (2015) Mechanics of collective unfolding. *Journal of the Mechanics and Physics of Solids* 76: 237–259.

Daynes S, Grisdale A, Seddon A, et al. (2014) Morphing structures using soft polymers for active deployment. *Smart Materials and Structures* 23: 012001.

Fok L, Ambati M and Zhang X (2008) Acoustic metamaterials. *MRS Bulletin* 33: 931–934.

Gomez JC and Garcia E (2011) Morphing unmanned aerial vehicles. *Smart Materials and Structures* 20: 103001.

Johnson DR, Thota M, Semperlotti F, et al. (2013) On achieving high and adaptable damping via a bistable oscillator. *Smart Materials and Structures* 22: 115027.

Klatt T and Haberman MR (2013) A nonlinear negative stiffness metamaterial unit cell and small-on-large multiscale material model. *Journal of Applied Physics* 114: 033503.

I Kovacic and MJ Brennan (eds) (2011) *The Duffing Equation: Nonlinear Oscillators and their Behaviour*. Chichester: John Wiley & Sons.

Kuder IK, Arrieta AF, Rathier WE, et al. (2013) Variable stiffness material and structural concepts for morphing applications. *Progress in Aerospace Sciences* 63: 33–55.

Lakes RS (2009) *Viscoelastic Materials*. Cambridge: Cambridge University Press.

Lakes RS and Drugan WJ (2002) Dramatically stiffer elastic composite materials due to a negative stiffness phase? *Journal of the Mechanics and Physics of Solids* 50: 979–1009.

Lakes RS, Lee T, Bersie A, et al. (2001) Extreme damping in composite materials with negative-stiffness inclusions. *Nature* 410: 565–567.

Lan G, Sartori P, Neumann S, et al. (2012) The energy-speed-accuracy trade-off in sensory adaptation. *Nature Physics* 8: 422–428.

Lindstedt SL, LaStayo PC and Reich TE (2001) When active muscles lengthen: properties and consequences of eccentric contractions. *News in Physiological Sciences* 16: 256–261.

Lombardi V, Piazzesi G and Linari M (1992) Rapid regeneration of the actin-myosin power stroke in contracting muscle. *Nature* 355: 638–641.

Marcucci L and Truskinovsky L (2010) Mechanics of the power stroke in myosin II. *Physical Review E* 81: 051915.

Nicolaou ZG and Motter AE (2012) Mechanical metamaterials with negative compressibility transitions. *Nature Materials* 11: 608–613.

Peraza-Hernandez EA, Hartl DJ, Malak RJJr, et al. (2014) Origami-inspired active structures: a synthesis and review. *Smart Materials and Structures* 23: 094001.

Philen M (2009) On the applicability of fluidic flexible matrix composite variable impedance materials for prosthetic and orthotic devices. *Smart Materials and Structures* 18: 104023.

Pontecorvo ME, Barbarino S, Murray GJ, et al. (2013) Bistable arches for morphing applications. *Journal of Intelligent Material Systems and Structures* 24: 274–286.

Puglisi G and Truskinovsky L (2000) Mechanics of a discrete chain with bi-stable elements. *Journal of the Mechanics and Physics of Solids* 48: 1–27.

Schultz MR (2008) A concept for airfoil-like active bistable twisting structures. *Journal of Intelligent Material Systems and Structures* 19: 157–169.

Shan Y, Philen M, Lotfi A, et al. (2009) Variable stiffness structures utilizing fluidic flexible matrix composites. *Journal of Intelligent Material Systems and Structures* 20: 443–456.

Shimamoto Y, Suzuki M, Mikhailenko SV, et al. (2009) Inter-sarcomere coordination in muscle revealed through individual sarcomere response to quick stretch. *Proceedings of the National Academy of Sciences of the United States of America* 106: 11954–11959.

Tolman SS, Delimont IL, Howell LL, et al. (2014) Material selection for elastic energy absorption in origami-inspired compliant corrugations. *Smart Materials and Structures* 23: 094010.

Tortora GJ and Derrickson BH (2006) *Principles of Anatomy and Physiology*. New York: John Wiley & Sons, Inc.

Wu Z, Harne RL and Wang KW (2015) Excitation-induced stability in a bistable Duffing oscillator: analysis and experiment. *Journal of Computational and Nonlinear Dynamics* 10: 011016.